Earth and Planetary Science Letters 594 (2022) 117710

Contents lists available at ScienceDirect

Earth and Planetary Science Letters

www.elsevier.com/locate/epsl

Ubiquitous dendritic olivine constructs initial crystal framework of mafic magma chamber

Chang-Ming Xing [a,b,c], Christina Yan Wang [a,b,c,*], Bernard Charlier [d], Olivier Namur [e]

[a] Key Laboratory of Mineralogy and Metallogeny, Guangzhou Institute of Geochemistry, Chinese Academy of Sciences, Guangzhou 510460, China
[b] CAS Center for Excellence in Deep Earth Science, Guangzhou 510640, China
[c] Guangdong Provincial Key Laboratory of Mineral Physics and Materials, Guangzhou 510640, China
[d] Department of Geology, University of Liège, 4000 Sart Tilman, Belgium
[e] Department of Earth and Environmental Sciences, KU Leuven, Heverlee 3001, Belgium

ARTICLE INFO

Article history:
Received 13 December 2021
Received in revised form 27 June 2022
Accepted 2 July 2022
Available online 19 July 2022
Editor: C.M. Petrone

Keywords:
olivine
phosphorus zoning
dendritic growth
cooling rate
Sept Iles layered intrusion

ABSTRACT

Layered intrusions are fossilized mafic magma chambers in the Earth's crust. The pathways that led to crystallization and solidification of layered intrusions have been hotly debated as the growth model of primocrysts (the earliest-formed crystals) in mafic magma chambers remains enigmatic. In this study, we carried out high-resolution elemental mapping of mm-scale olivine primocrysts from the Sept Iles layered intrusion (Canada), the third largest one in the world, with a focus on phosphorus (P) zoning of olivine. Our results reveal that complex P zoning of olivine with intense dissolution textures is ubiquitous in the ~4.7 km-thick Layered Series of the intrusion. The P-rich zones of olivine are featured with dendritic, hopper and sector-zoned patterns, which are attributed to significant magma undercooling. Thermal modeling based on a 1-D conductive cooling model suggests that initially hot parental magma intruding into cold country rocks would result in high degrees of undercooling ($-\Delta T$ >60 °C) in the margins (*i.e.*, floor, roof and sidewalls) of magma chamber, facilitating rapid growth of dendritic olivine, which may be then spread within the magma chamber by dynamic convection and crucial to construct initial crystal framework of a solidifying magma chamber. Additionally, diffusion modeling based on the P gradients in olivine suggests a minimum cooling rate of 2.7 to 3.3×10^{-3} °C/year in the center of the intrusion, similar to the averaged cooling rate of other layered intrusions (e.g., Bushveld, Stillwater and Skaergaard) reported in previous studies. This indicates that rapid cooling (ca. 10^{-2} to 10^{-3} °C/year) at high temperature (>800 °C) may be predominant regardless of the size of magma chambers. Our study demonstrates that P zoning of olivine is powerful in decoding crystallization and thermal histories of mafic-ultramafic intrusions.

1. Introduction

Magma crystallization and solidification in crustal magma chambers are key processes to our understanding of igneous differentiation, magmatic ore deposit formation and volcanic eruption. A classic model in igneous petrology relies on a premise that a crustal magma chamber is melt-dominated, and that crystallization begins with the development of mushy layers on cold margins and progresses towards the center of magma chamber (McBirney, 1996; Irvine et al., 1998; Holness et al., 2007; Namur et al., 2011; Latypov et al., 2020, 2022). However, geophysical, geochemical and petrological observations on active volcanos worldwide suggest a transcrustal magmatic system in which crystal mushes are dominating and melt-rich portions occur as stacked melt lenses (Cashman et al., 2017; Sparks and Cashman, 2017). Although voluminous melt in crustal magma chamber is thought to be physically unstable and thus short-lived (Cashman et al., 2017), it remains unclear how long it takes to generate an initial crystal mush in a magma chamber. The missing link between these models can be made by understanding how initially a crystal mush develops in a magma chamber. Answering these questions requires a good comprehension of crystallization mechanism and growth rate of primocrysts in a magma chamber.

Layered intrusions are fossilized magma chambers that preserve stunning records of differentiation pathways of basaltic magmas from the mantle via storage in crustal magma chambers to eruption (Wager and Brown, 1968). The cooling rate of magma and

* Corresponding author at: Key Laboratory of Mineralogy and Metallogeny, Guangzhou Institute of Geochemistry, Chinese Academy of Sciences, Guangzhou 510460, China.
E-mail address: wang_yan@gig.ac.cn (C.Y. Wang).

https://doi.org/10.1016/j.epsl.2022.117710
0012-821X/

the degree of undercooling ($-\Delta T = T_{liquidus} - T_{crystallization}$) in layered intrusions are usually unknown but can strongly affect crystal nucleation and growth rate, crystal growth mechanism and morphology, and chemical compositions and textures of rocks (Faure et al., 2003, 2007; Shea and Hammer, 2013). Valuable information on magma crystallization and cooling may however be preserved in the chemical zoning of minerals (Streck, 2008; de Maisonneuve et al., 2016). Cracking the secrets in the chemical zoning of primocrysts from layered intrusions may throw critical constraints on the formation of crystal mush and cooling history of magma chambers.

Phosphorus (P) diffuses extremely slowly compared to other major and trace elements in olivine (Watson et al., 2015), making P in olivine a potential recorder of cooling history of a magma chamber. Dendritic pattern of P zoning in olivine has been widely documented in volcanic rocks (e.g., Milman-Barris et al., 2008; Welsch et al., 2013, 2014), which is attributed to initially rapid growth of P-rich dendrites followed by slow ripening and infilling of P-poor domains, *i.e.*, dendritic model of crystal growth (Welsch et al., 2013, 2014). However, this texture is rarely examined in plutonic rocks (Welsch et al., 2014; Xing et al., 2017; Mao et al., 2022). In this study, we carried out high-resolution elemental mapping of olivine from the Sept Iles layered intrusion in Canada, with a focus on its P zoning. Our results show remarkably complex P zoning with distinct disequilibrium textures in millimeter-scale olivine grains throughout the Layered Series of the intrusion, revealing ubiquitous dendritic growth of olivine and late-stage dissolution-reprecipitation processes. This study indicates that the complex P zoning of olivine primocrysts from layered intrusions can provide a new perspective on the crystallization and cooling histories of mafic magma chambers.

2. Sept Iles layered intrusion

The Sept Iles intrusion in Canada is the third largest layered intrusion after the Bushveld Complex in South Africa and the Dufek intrusion in Antarctica (Namur et al., 2010). It is a circular plutonic body, ca. 80 km in diameter, ca. 5.5 km in thickness and ca. 20,000 km^3 in volume (Loncarevic et al., 1990) (Fig. 1A). The intrusion was dated to be 564±4 Ma and considered to be associated with a mantle plume (Higgins and van Breemen, 1998) or lithospheric reorganization (Namur et al., 2010). The intrusion comprises, from the base upwards, a fine-grained gabbroic Border zone, a troctolitic and gabbroic Layered Series, an anorthositic Upper Border Series and a granitic Upper Series (Fig. 1B; Higgins, 2005). The Layered Series is at least 4.7 km in thickness and is further divided into three megacyclic units (MCU), namely MCUs I, II and III (Fig. 1C; Namur et al., 2010). The Layered Series hosts economic resources of Fe, Ti, P and V, including >24 layers of cm- to meter-scale Fe-Ti oxide ore and two ca. 200-m-thick apatite-rich macrolayers. Olivine and plagioclase are two major primocrysts throughout the Layered Series except for relatively thin olivine-free zones in MCU I and MCU II (Namur et al., 2010).

Previous studies on the Sept Iles intrusion reveal that progressive fractional crystallization of the parental magma is interrupted by two major magma replenishment events marking the base of MCUs II and III, respectively, and at least six small magma inputs during crystallization of MCU II (Fig. 1D; Namur et al., 2010). Such mixing events result in multiple reversals of mineral compositions towards more primitive values, e.g., olivine Fo and clinopyroxene Mg# (Fo/Mg# = 100×Mg/(Mg+Fe) molar), plagioclase An (An = 100×Ca/(Ca+Na) molar) and magnetite Cr content, forming distinct "mixing zone" at a scale of 25-120 m (Fig. 1D; Namur et al., 2010). Differentiation of magmas between these "mixing zones" is dominated by fractional crystallization even though silicate liquid immiscibility developed during crystallization of the apatite-rich "critical zone" at the top of MCU II (Charlier et al., 2011; Namur et al., 2012). Silicate liquid immiscibility in the mush liquid of the Layered Series is revealed by widespread replacive symplectites (Keevil et al., 2020). Anorthosite of the Upper Border Series (UBS) has been formed by plagioclase flotation during early fractionation of MCU I (Higgins, 2005; Namur et al., 2011). The anorthosite in MCU I, however, is anorthosite autolith that sank from UBS, and mafic minerals (e.g., olivine and pyroxene) in the anorthosite crystallized from interstitial liquid among plagioclase crystals (Namur et al., 2011).

3. Analytical methods

Fresh olivine grains were selected from ten samples that were collected from the Layered Series of the Sept Iles intrusion, including troctolite and massive Fe-Ti oxide ore in the lower part of MCU I, troctolite and gabbro in the middle part of MCU I, apatite olivine gabbro at the top of MCU I, olivine gabbro and net-textured Fe-Ti oxide ore in the lower part of MCU II, apatite troctolite and olivine nelsonite at the top of MCU II (Fig. 1C and Supplementary Fig. 1). Two anorthosite samples in MCU I were also selected for comparison. Overall, our samples are representative of the crystallization products of magma evolution in different areas and stages of the magma chamber.

3.1. Measurement of mineral modes

High-resolution, colored scan images for each thin sections were obtained by using a Leica DVM6 digital microscope, which is equipped with an automatic sample stage and connected to a computer. The scan images were then inverted to 8-bit greyscale images so that the total area of opaque minerals (Fe-Ti oxides and sulfides) and major transparent minerals (olivine, plagioclase, clinopyroxene, apatite) can be measured on the greyscale images by using image processing software of ImageJ (version 1.44p) (https://imagej.nih.gov/ij/). Olivine, plagioclase and clinopyroxene grains were outlined on the colored image, respectively, and then measured by ImageJ to obtain their proportions separately. For each thin section, an area of 15-25 mm × 25-30 mm was counted to cover all minerals.

3.2. Elemental quantitative analysis

Major and trace elements of olivine were analyzed by a JEOL JXA-8230 electron probe micro-analyzer (EPMA), which is equipped with five wavelength-dispersive spectrometers, at the Key Laboratory of Mineralogy and Metallogeny in Guangzhou Institute of Geochemistry (GIG), Chinese Academy of Sciences (CAS). Operating conditions of 15 kV, 50 nA and a 1 μm beam were applied to the analyses for all elements. Peak and upper/lower background counting times were 20 and 10 seconds for Si, Fe, Mg, 60 and 30 seconds for Ca, 90 and 45 seconds for Mn and Ni, 160 and 80 seconds for P, 180 and 90 seconds for Al. Analytical results were reduced using the ZAF correction routines. The standards used for calibration were olivine for Si and Mg, magnetite for Fe, Cr-diopside for Ca, apatite for P, almandine garnet for Al, rhodonite for Mn and Ni metal for Ni. Before routine analysis, an olivine standard from SPI Supplies was analyzed repeatedly to monitor data quality. According to 10 analyses for the olivine standard, relative precisions are better than ±2% for Si, Fe and Mg and ±5% for Ni, respectively. The accuracy and precision of P measurement is <7% and <15%, respectively, based on repeated analyses (n=32) of the olivine reference standard MongOL Sh11-2 that contains 66.4±20 (2σ) ppm P (Batanova et al., 2019). The detection limit for P yielded by JEOL EPMA software is about 21 ppm.

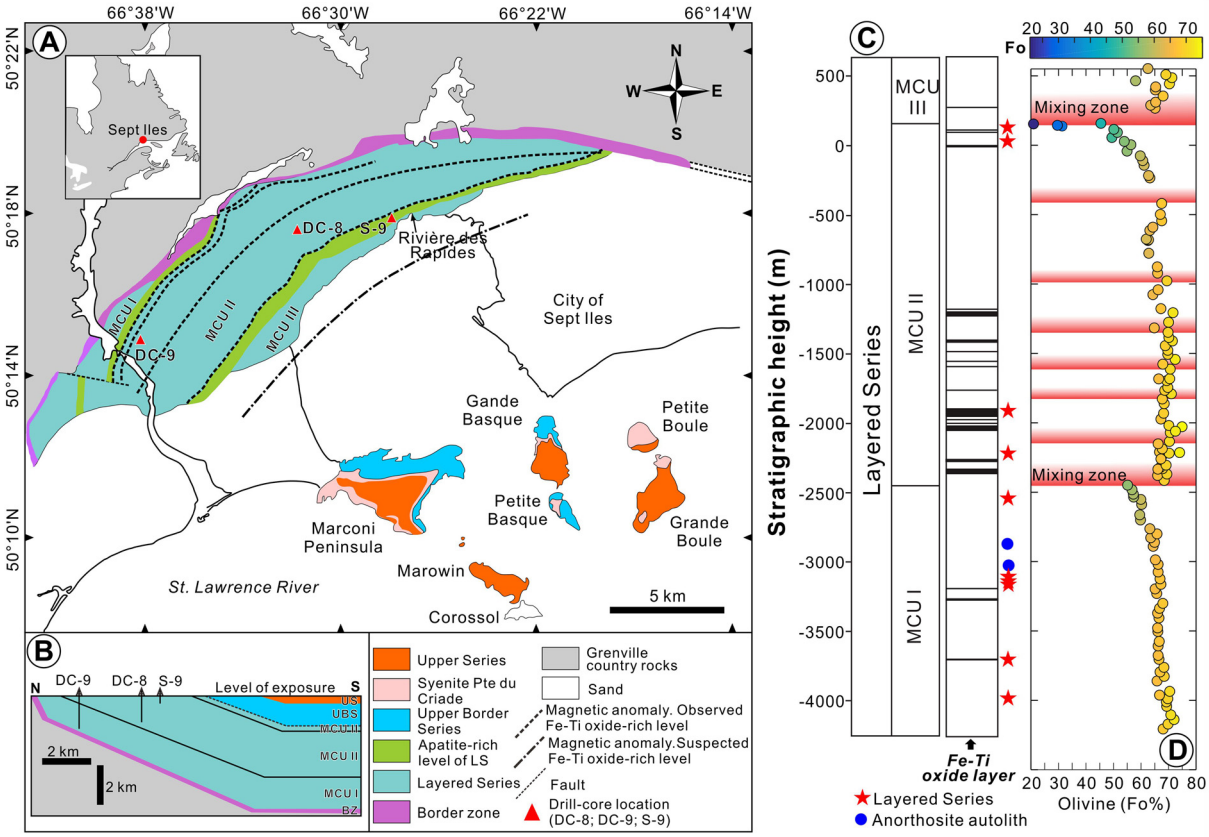

Fig. 1. Geological map of the Sept Iles layered intrusion and stratigraphic column of the Layered Series. (**A**) A sketched geological map showing the distribution of subdivision of the intrusion (modified after Namur et al., 2010). The inset shows its location in Canada. (**B**) A cross-section showing the intrusion comprises the Border zone (BZ), Layered Series (MCUs I, II and III), Upper Border Series (UBS) and Upper Series (US). (**C**) A stratigraphic column of the Layered Series showing three megacyclic units (MCU) of I, II and III, main Fe-Ti oxide layers and sample locations. (**D**) Variation of olivine Fo content along the stratigraphic column (modified after Namur et al., 2010). Magma "mixing zone" in MCUs II and III are adopted from Namur et al. (2010). The locations of three drill-cores (DC-8, DC-9 and S-9) are shown in (A) and (B).

Major elements of plagioclase were analyzed by the EPMA with operation conditions of 15 kV, 20 nA and a 1 μm beam. The standards used were plagioclase for Si and Al, albite for Na, Cr-diopside for Ca, K-feldspar for K, magnetite for Fe, and rutile for Ti. Na and K were measured at first to minimize their loss during analyses. The peak and upper/lower background counting time were 10 and 5 seconds for Na and K, 20 and 10 seconds for Si, Al and Ca, 40 and 20 seconds for Fe and Ti.

3.3. Elemental mapping and line scan analysis

Elemental mapping for P, Mg, Al, Ca, Cr and Ni of olivine grains were carried out on carbon-coated thin sections using the EPMA. The operation conditions of an accelerate voltage of 20 kV, a probe current of 500 nA and a beam size of 3-4 μm were adopted for elemental mapping. Mg and Al were analyzed using a TAP crystal. Ca was analyzed using a PET crystal. P was analyzed either by a single PETH crystal in one spectrometer or by two PETJ crystals and one PETH crystal in three spectrometers to enhance signal/background ratios. Elemental Kα line was chosen for all elements during analyses. The step size was 3 or 4 μm and the dwell time was set to be 150-200 ms for each point. It took ca. 5-22 hours to obtain elemental maps for a single olivine grain.

Profiles of P X-ray intensity were obtained using the same EPMA. A PETH crystal was used for P intensity analysis. The operation conditions of an acceleration voltage of 20 kV, a probe current of 500 nA and a beam of spot mode (<1 μm) were adopted for all profiles. The step size was set to be 0.1-0.2 μm and the dwell time was increased to 1000 ms for each point. For each profile, the P intensities were obtained by repeated scanning with an accumulation number of 5 to enhance signal/noise ratios.

3.4. Crystallographic orientation analysis

Crystallographic orientation of olivine was determined by the Oxford Symmetry electron backscatter diffraction (EBSD), which is equipped onto a Zeiss Sigma 300 field emission scanning electron microscope (FE-SEM) at Institute of Materials and Processing, Guangdong Academy of Sciences. Thin sections were carbon-coated to reduce electron charging effect. The measurements were conducted with an acceleration voltage of 20 kV and a working distance of ~20 mm. The thin sections were tilted 70° and Kikuchi patterns were acquired on rectangular grids by shifting the electron beam with a step size of 10-20 μm. Olivine ((100)=4.756Å, (010)=10.207Å, (001)=5.980Å, α=90°, β=90°, γ=90°) was adopted for EBSD index. Raw EBSD data clean up and post-processing were performed in MTEX (Bachmann et al., 2010), an open-source toolset for MATLAB software.

3.5. Thermal modeling

To constrain the degree and scale of undercooling during initial magma emplacement, thermal diffusion was modeled assuming conductive cooling in a stationary mode. Thermal modeling was carried out using the Fourier's Law of heat conduction in 1-dimensional formula (Di Maio et al., 2015):

$$\frac{\partial}{\partial z}\left(k\frac{\partial T}{\partial z}\right) = \rho C_P \frac{\partial T}{\partial t} \quad (1)$$

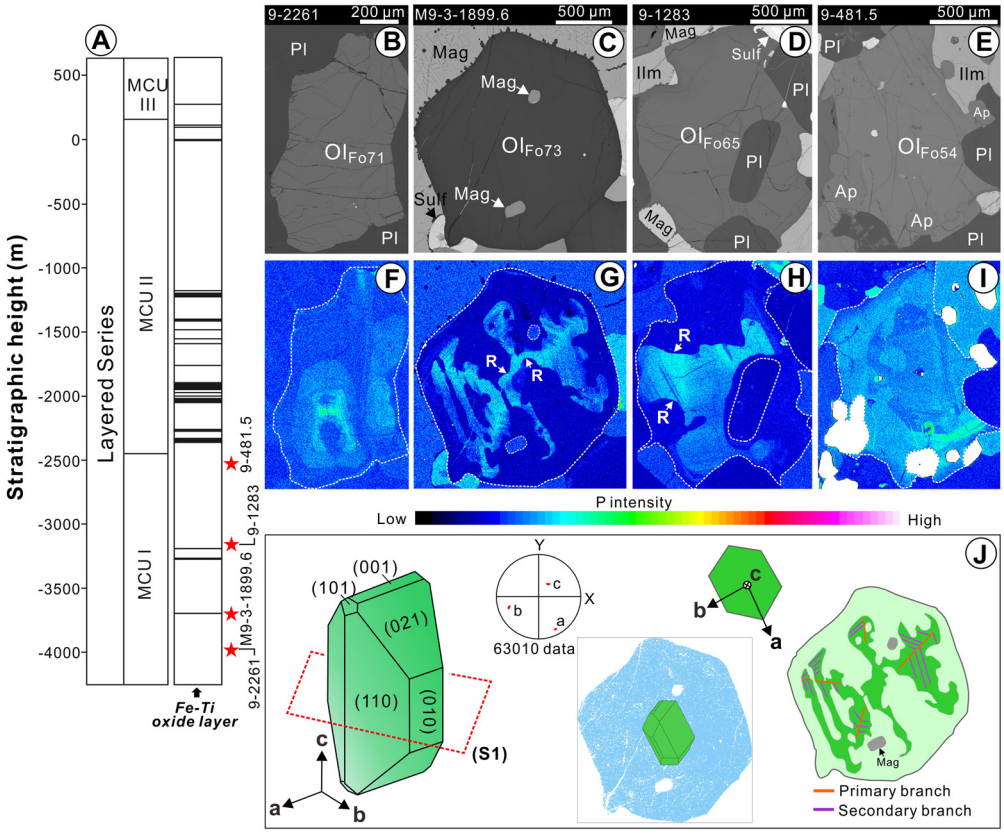

Fig. 2. Phosphorus zoning patterns of olivine from MCU I of the Sept Iles layered intrusion. (**A**) The sample locations in the stratigraphic column. (**B-E**) Back-scattered electron images of olivine (Ol) grains. Magnetite (Mag), plagioclase (Pl) and apatite (Ap) inclusions are enclosed in olivine. (**F-I**) Phosphorus maps of olivine grains showing diverse, complex P zoning patterns with intense dissolution. The P-rich zones are generally enclosed within broadly P-poor domains and occur as hopper (F), dendritic (G), sector-zoned (H) and irregular patches (I) in olivine. The major resorption surface (R) is featured by distinct embayment and irregular boundaries of P-rich zones (Fig. 2G-H). Magnetite and plagioclase are enclosed within the P-poor domains. Apatite grains are partially enclosed within the olivine rim (I). (**J**) Electron back-scattered diffraction (EBSD) map of the olivine grain in (G) showing crystallographic orientation of olivine. The lower hemisphere equal area projection of crystallographic axes is shown in the insets. The 3D olivine crystal model on the left is modified from Welsch et al. (2013). The 3D olivine crystal model is superimposed on the EBSD map using the MTEX toolbox for MATLAB (Bachmann et al., 2010). The cross section of S1 and sketches of P zoning showing primary branches at crystal corners and secondary branches along crystal planes.

where k is the thermal conductivity ($W \bullet m^{-1} \bullet K^{-1}$), ρ is the density ($kg \bullet m^{-3}$), C_p is the heat capacity ($J \bullet kg^{-1} \bullet K^{-1}$), T is temperature (K), z is distance (m), t is time (s). The equation was solved by finite difference method using MATLAB software. The parameters used in the thermal modeling are shown in Supplementary materials.

3.6. Measurement on midpoint slope (S_0) of P gradients in olivine

To confine the sharpness of P gradients for the P-rich bands in olivine and to quantify the timescale required to preserve the observed P gradients, we measured the midpoint slope (S_0, slope of a normalized diffusion profile; cf., Watson and Cherniak, 2015) for the outer (toward the rim of olivine) and inner (toward the core of olivine) boundaries of P-rich bands, following Watson and Cherniak (2015) and Tang et al. (2017). On one hand, S_0 can be measured on the basis of the normalized profiles (Tang et al., 2017):

$$S_0 = \frac{50\%}{l} \tag{2}$$

where l is the diffusion distance from 25% to 75% of the normalized P gradients. On the other hand, the S_0 can be modeled using following equation (Watson and Cherniak, 2015):

$$S_0 = \frac{28.21}{\sqrt{D_P \Delta t}} \tag{3}$$

where D_P is the diffusivity of P in olivine and Δt is the diffusion timescale.

3.7. Diffusion modeling on the basis of P gradients in olivine

The diffusion modeling for X-ray P intensity profiles of olivine was conducted using Fick's Second law in one dimension (Crank, 1975):

$$\frac{\partial C_P}{\partial t} = \frac{\partial}{\partial x}\left(D\frac{\partial C_P}{\partial x}\right) \tag{4}$$

where C_P is X-ray intensity of P, D is diffusion coefficient (m^2/s), t is time (s), x is distance (m). The diffusion equation was solved by finite difference method using MATLAB software. The X-ray intensity profiles of P in olivine were firstly fitted by nonlinear least squares regression (NLSR) method and then the fitted curves were used for diffusion modeling. A total of 240-600 grid points were used depending on the length of each P profiles. The "best fit" was obtained using the minimum root mean squares (rms) method (Girona and Costa, 2013).

4. Results

4.1. Fo contents of olivine

The olivine grains overall account for 2 to 32 vol.% of the samples from the Layered Series (Supplementary Table 1). They typi-

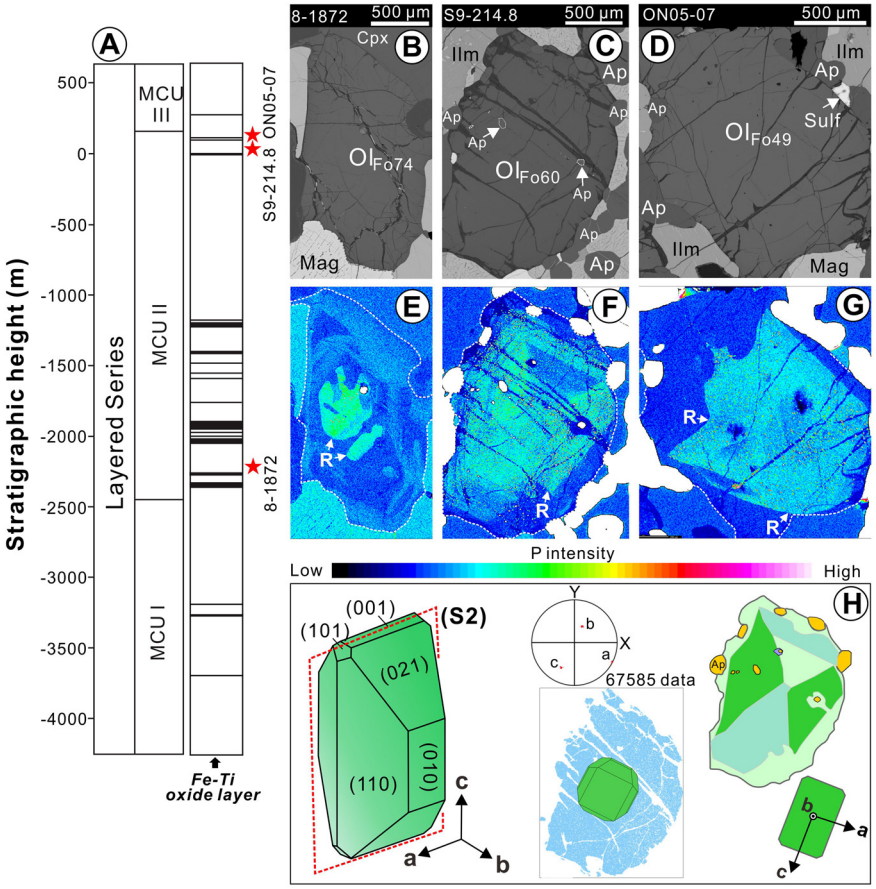

Fig. 3. Phosphorus zoning patterns of olivine from MCU II of the Sept Iles layered intrusion. (**A**) The sample locations in the stratigraphic column. (**B-D**) Back-scattered electron images of olivine (Ol) grains. (**E-G**) Phosphorus maps of olivine grains showing complex patterns of P-rich zones, occurring as multiple patches (E), sector zoning (F) and irregular domains (G) in olivine. These patterns are similar to those of olivine in MCU I. (**H**) EBSD map of the olivine grain in (F) showing crystallographic orientation of olivine. The lower hemisphere equal area projection of crystallographic axes is shown in the insets. The cross section of S2 and sketches of P zoning showing sector-zoned olivine with relatively large apatite grains partially enclosed within the olivine rim.

cally range in size from 1 to 5 mm, and have Fo contents varying from 74 to 49 (Supplementary Table 2). For a single olivine grain, Fo contents in the rim part generally increase by 1 to 5 unit compared to that in the core part (Supplementary Table 2). The olivine grains in the anorthosite of MCU I are generally 2 to 5 mm in size and account for ~3 vol.% of the rocks. Olivine grains in two anorthosite samples have Fo contents varying from 62 to 65 (Namur et al., 2011).

4.2. Phosphorus zoning of olivine

The olivine grains that were observed in the thin sections of all the samples from the Layered Series do not show clear zoning under backscattered electron (BSE) images (Fig. 2B-E, Fig. 3B-D and Fig. 4C-D) and cross-polarized microphotographs (Supplementary Fig. 1). However, they all show distinct, complex zoning patterns in high resolution P maps (Figs. 2F-I, 3E-G and 4E-F and Supplementary Figs. 2-3). Overall, the P-rich zones in olivine contain 200 to 450 ppm P, whereas the P-poor domains in olivine contain 50 to 145 ppm P (Supplementary Table 2). They locally show concentric zoning of Mg and Ca but have uniform distribution of Al, Cr and Ni (Supplementary Fig. 4). In contrast to what is observed in most samples from the Layered Series, the olivine grains in anorthosite do not show clear P zoning (Supplementary Fig. 5).

Generally, the P-rich zones of olivine in the Layered Series are enclosed within broad P-poor domains and occur as diverse patterns (Figs. 2 and 3). Olivine grains from MCU I show distinct hopper (Fig. 2F) and dendritic (Fig. 2G) P-rich zones, incomplete sector zoning (Fig. 2H) and irregular P-rich patches (Fig. 2I and Supplementary Fig. 2). In the hopper pattern, V-shaped cavities develop with P-rich, tabular domain at the center of two cavities, which are occupied by P-poor domains (Fig. 2F). In the dendritic pattern, the P-rich zones occur as fishbones with primary branches at crystal corners and secondary branches along crystal plane (Fig. 2G and J). The boundaries between P-rich zones and P-poor domains are commonly irregular and the linear extension of P-rich zones along the crystal plane can be suddenly truncated by P-poor domains, forming a distinct embayment texture (Fig. 2G-H). In addition, inclusions of magnetite and plagioclase are exclusively located within the P-poor domains of olivine (Fig. 2G-H). Olivine grains from MCU II show similar patterns of P-rich zones, which also exhibit irregular boundaries and rounded edges at crystal corners (Fig. 3E-G and Supplementary Fig. 3). In the sector-zoned olivine from nelsonite of MCU II, fine-grained apatite grains are enclosed within the prism sectors (e.g., {1 1 0} and {$\bar{1}$ $\bar{1}$ 0}), whereas relatively coarse-grained apatite grains are partially enclosed within the P-poor rim of the olivine (Fig. 3F and H).

Olivine grains from net-textured Fe-Ti oxide ore of MCU II are rounded in morphology (Fig. 4B), but the P-rich zones of olivine show dendritic (Fig. 4E) or incomplete, polygonal shape (Fig. 4F). A rounded olivine grain shows well-preserved delicate oscillatory zoning of P, which comprises multiple, concentric P-rich bands (<10 to 200 μm in width) alternating with μm-scale P-poor zones (Fig. 5A). The primary P-rich branches are missing in the map, which is likely because all crystal corners of the grain cannot be seen in the 2-D cutting plane (Fig. 5B-C). The results of X-ray line

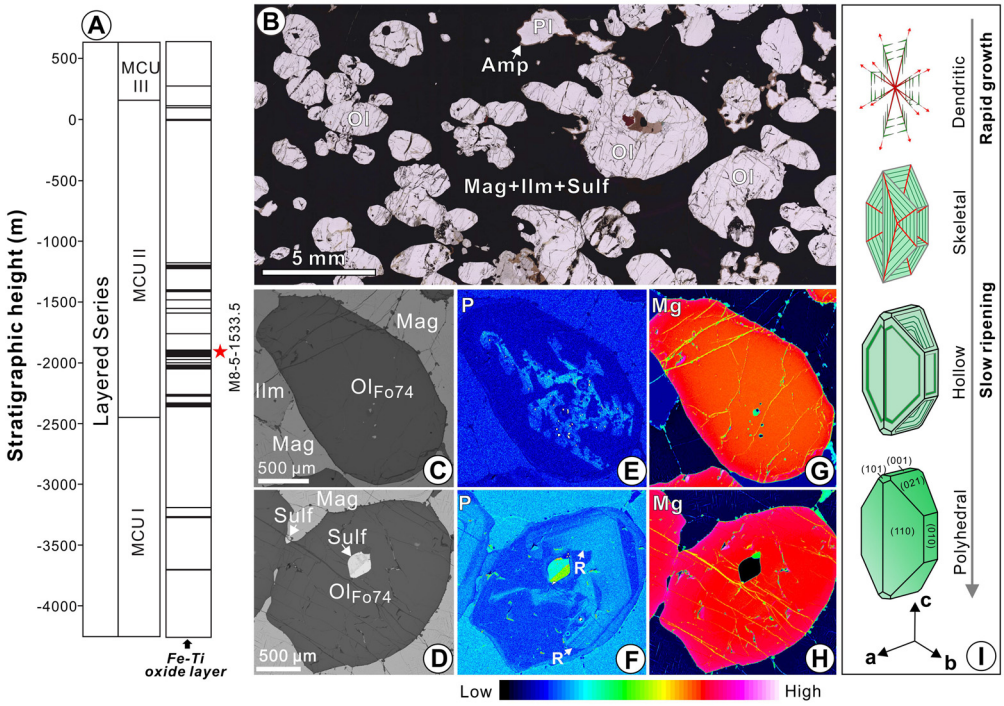

Fig. 4. Elemental maps of olivine in net-textured Fe-Ti oxide ore of MCU II. (**A**) Sample location in the stratigraphic column. (**B**) Scanned image of the thin section showing that rounded olivine grains are surrounded by a matrix of magnetite (Mag) + ilmenite (Ilm) and sulfide (Sulf). Plagioclase (Pl) is irregular in shape and commonly rimmed by amphibole (Amp). (**C-D**) Back-scattered electron images of olivine grains. (**E-F**) Phosphorus maps of olivine grains showing complex P zoning with dendritic (E) or polyhedral (F) P-rich zones despite of intense dissolution (the major resorption surface is marked as "R"). (**G-H**) Magnesium maps of olivine grains showing slightly concentric zoning in the rim. (**I**) A sketch showing the dendritic growth model of olivine, modified after Welsch et al. (2013) and Shea et al. (2019). Dendritic growth of olivine initiates with development of primary branches from the crystal center towards the apexes of olivine, followed by secondary branches along crystal planes. Subsequently, overgrowth and back-filling of P-poor domain on dendritic olivine develop polyhedral olivine.

scan show sharp P gradients and asymmetric patterns across the boundaries of P-rich bands and P-poor domains (Fig. 5D-F). For P-rich bands with a wide (>20 μm), high plateau, the P gradient of outer boundary (toward the rim of grain) is generally steeper than that of inner boundary (toward the core of grain) (Fig. 5E). The asymmetric boundaries are even more prominent for the thin bands with tapering plateau (Fig. 5F). Extremely narrow P-rich bands (<10 μm) between thick bands generally lack a high plateau (shown as an open rectangle in Fig. 5E-F).

5. Discussion

5.1. Undercooling of the Sept Iles intrusion

Experimental studies demonstrate that there is a systematic change of olivine morphologies from polyhedral habit to hopper/skeletal habit and then to dendritic habit as a function of increasing cooling rate and degree of undercooling (Donaldson, 1976; Jambon et al., 1992; Faure et al., 2003, 2007; Mourey and Shea, 2019). At low cooling rate, polyhedral olivine crystallizes through a tree-ring growth model and the growth process is interface-controlled. At moderate degrees of undercooling and fast cooling, hopper crystals with V-shaped cavities develop through skeletal growth model and the growth process is diffusion-controlled. At high degrees of undercooling and fast cooling, dendritic olivine forms through dendritic growth model and the growth process is also diffusion-controlled (Faure et al., 2003, 2007; Faure and Schiano, 2005; Welsch et al., 2013).

Olivine grains from the Layered Series are characterized by dendritic pattern of P zoning (Fig. 2G and 4E), hinting dendritic growth model of olivine (Welsch et al., 2013, 2014). Some olivine grains also show hopper (Fig. 2F) and sector zoning (Figs. 2H and 3F) of P-rich zones, indicating skeletal growth model of olivine (Faure et al., 2003, 2007). The diversity in the textural patterns of P-rich zones of the olivine observed in this study thus can be attributed to multiple growth models of olivine as well as the cutting effect on the olivine grains that have different crystallographic orientations, which are revealed by electron backscattered diffraction (EBSD) results (Figs. 2J, 3H and 5B).

Previous experimental studies demonstrated that dendritic growth of olivine requires high degrees of undercooling (-ΔT >60 °C) and fast cooling (>47 °C/h) of magmas (Donaldson, 1976; Jambon et al., 1992; Faure et al., 2003, 2007). Such a high thermal gradient may occur in the margin of a large magma chamber (Welsch et al., 2013). However, new experimental results reveal that low-to-moderate degrees of undercooling (-ΔT=25-60 °C) are sufficient to the skeletal or dendritic growth of olivine, producing P zoning patterns that resemble those observed in natural olivine grains (Shea et al., 2019; Mourey and Shea, 2019). Such low to moderate degrees of undercooling can be created by magma mixing in crustal magma chambers (Shea et al., 2019). The hotter recharging magma could be undercooled by several tens of degrees at the contact of previously formed cumulates and relatively cold residual melt. This is particularly illustrated by intraplutonic quench zones at the bases of 12 macrorhythmic units of the Kap Edvard Hom complex in Greenland and the presence of cm-scale olivine dendrites in the poikilitic cumulates overlying the quench zones, which was interpreted as magma recharging along the magma chamber floor with -ΔT of ~40-50 °C (Tegner et al., 1993; Tegner and Wilson, 1995). Given that the Layered Series of the Sept Iles intrusion was frequently recharged by hot, primary magma during the formation of MCU II (Namur et al., 2010), we suggest that magma undercooling due to recharges may have played a significant role in developing P zoning of olivine in the magma chamber.

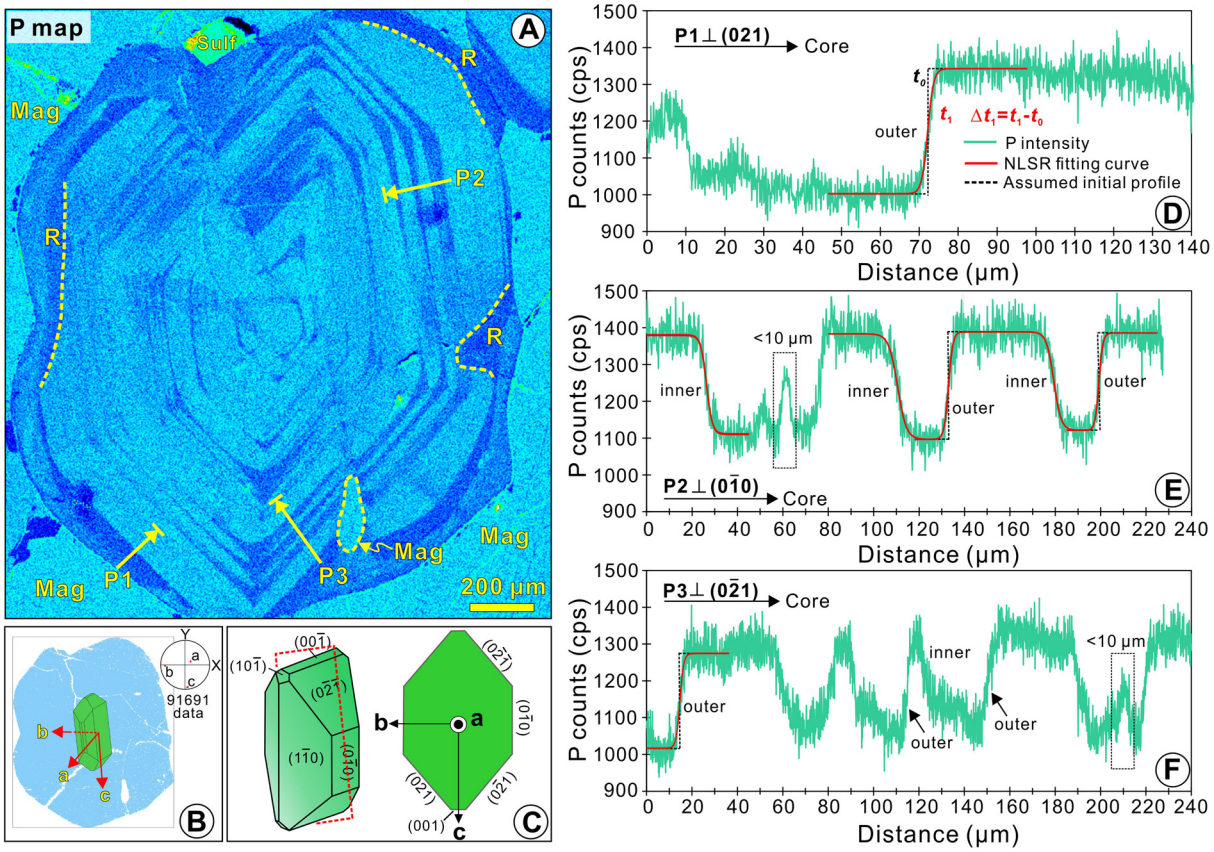

Fig. 5. Phosphorus intensity map and profiles of an olivine grain in net-textured Fe-Ti oxide ore of MCU II. (**A**) P map showing delicate oscillatory zoning of P of the grain. The P-rich zones occur as multiple, concentric bands with variable thickness and are partially dissolved by P-poor domains, forming distinct resorption surface (R). Note the discontinuity of P-rich zones at crystal corners between {02 1} and {0$\bar{2}$ 1}. (**B**) The EBSD map of the grain, the inset showing lower hemisphere equal area projection of crystallographic axes. A 3-D olivine crystal model is superimposed on the EBSD map using MTEX toolbox. **(C)** A sketch showing the cross section of a 3-D olivine, which is modified from Welsch et al. (2013). (**D-F**) Phosphorus line scan profiles across different crystal planes of the grain. Note the asymmetric distribution of P gradients in the outer and inner boundaries of P-rich bands. Raw P intensity profiles of the boundaries were fitted using non-linear least squares regression (NLSR) method.

To estimate the potential extent of magma undercooling in the formation of the Layered Series of the Sept Iles intrusion, the liquidus temperature of magma was calculated using compositions of plagioclase in the rocks (Namur et al., 2010) and empirical plagioclase thermometer of Thy et al. (2009, 2013) that was initially used to calibrate the liquidus temperature of the Skaergaard layered intrusion in Greenland. This method is appropriate because both the Skaergaard and Sept Iles intrusions have ferrobasaltic parental magmas with similar bulk Mg# (51 and 49, respectively) and comparable crystallization sequences (Namur et al., 2010).

In this study, the liquidus temperature of magma was calculated using empirical plagioclase thermometer of T(°C) = 933 + 3.2An (1σ = ±18 °C) (Thy et al., 2013). The results show that the temperature difference caused by two major magma recharging events at the base of MCUs II and III is up to 48 to 120±18 °C (1σ), and those by small magma inputs within MCU II vary from 3 to 21±18 °C (1σ) (Supplementary Fig. 5), indicating that variable degrees of undercooling may occur in the magma chamber. Given the sampling interval of Namur et al. (2010) is in decameter-scale, the results may represent the minimum temperature differences.

The ~1.8-km-thick MCU I is considered to have formed from progressive differentiation of a single batch of ferrobasaltic magma and unaffected by magma mixing (Fig. 1D; Namur et al., 2010). Thus, undercooling that resulted in skeletal and dendritic growth of olivine in MCU I was likely caused by the temperature difference between hot magma and cold country rocks. Given the thickness of MCU I, we suggest that MCU I cannot be wholly undercooled and particularly, olivine grains with dendritic P zoning in the middle part of MCU I may initially form in the margins of the chamber, *i.e.*, floor, roof or sidewalls, even though it is difficult to identify the exact place where these grains initially formed. Here, we propose a possible model involving accumulation of rapidly-growing olivine at the floor and continuous crystallization of olivine at the roof to illustrate their formation. When hot magma were initially emplaced into cold country rocks, the forced, turbulent convection may cause rapidly-growing olivine crystals at the floor and roof spreading and suspending in the magma chamber (*e.g.*, Yao et al., 2021). However, the vigorous momentum of turbulent convection may be gradually dissipated once the intrusion of magma ceased, leading to suspending crystals to settle down on the floor. As crystals eventually piled up on the floor, the thermal gradients of magma can be significantly reduced so that undercooling cannot be generated for dendritic growth of olivine in the overlying magma. On the other hand, olivine grains may also grow rapidly at roof and form an olivine-rich plume, which may descend quickly towards the bottom of magma chamber, resulting in ubiquitous distribution of olivine crystals throughout the interior of MCU I (e.g., Brandeis and Jaupart, 1986; Morse, 1986). Therefore, it is accumulation of the rapidly-growing olivine on the floor and continuous crystallization of olivine at roof that eventually resulted in widespread distribution of dendritic olivine in MCU I.

In summary, degrees of undercooling in the Layered Series were likely variable in the magma chamber and could be induced by either cold country rocks or magma replenishment. The hopper, dendritic and sector patterns of P zoning observed in the olivine of the Layered Series could be attributed to the variable degrees of magma undercooling.

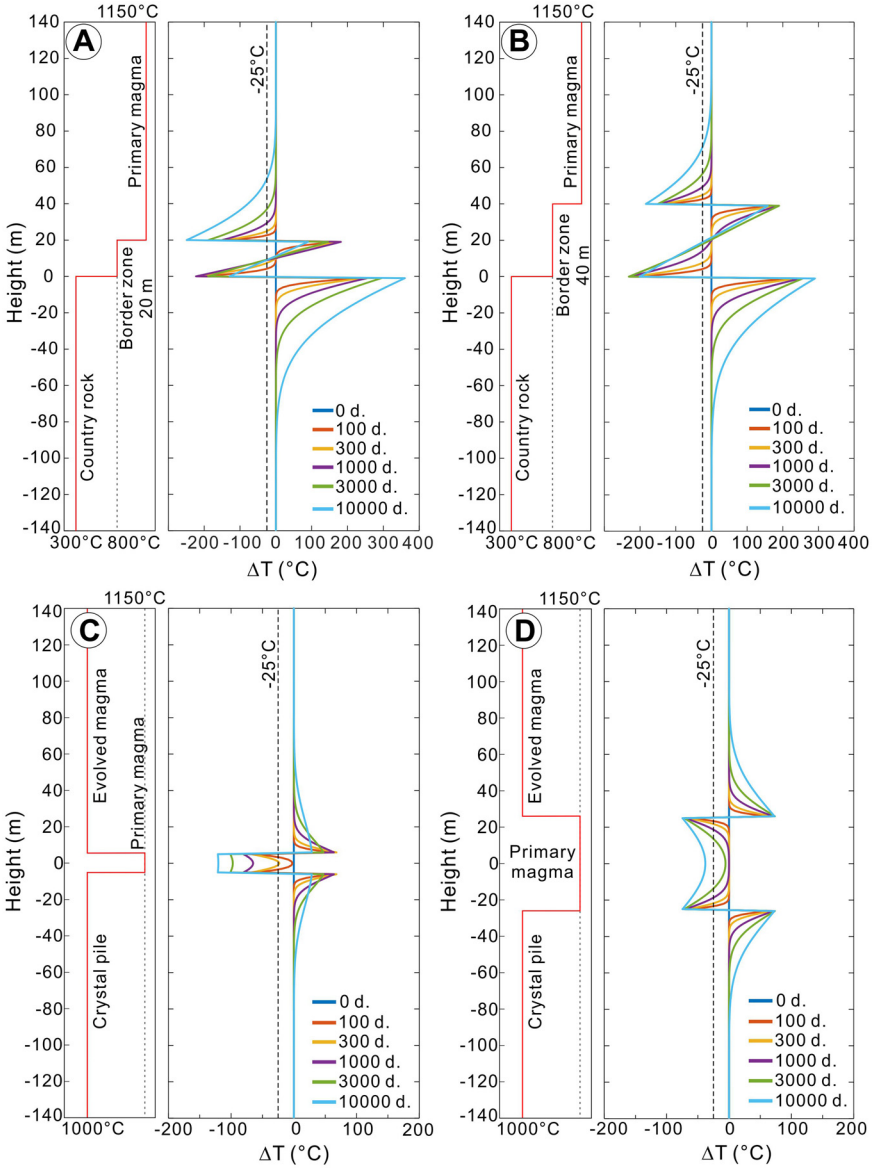

Fig. 6. Numerical modeling on 1D conductive cooling of magma. (**A-B**) Initially hot, primary magma intrudes cold, metamorphic country rocks with a 20/40 m-thick border zone between them. The temperature of primary magma was set to be 1150 °C (Namur et al., 2010). The temperature of the country rocks and border zone was estimated to be 300 °C and 800 °C, respectively. Thermal modeling was carried out using 1D thermal conduction equation (Di Maio et al., 2015). The results show that high degrees of undercooling (>100 °C) can be quickly developed at the base of magma in 100 days. In addition, the thickness of magma affected by -ΔT >25 °C undercooling at 10000 days is similar regardless of the thickness of the border zone. (**C**) A 10-m-thick primary magma layer intrudes the base of cooler (1000 °C), evolved magma. The results show that the whole-part of intruding magma layer can be cooled down by 23 to 67 °C in 300 days. (**D**) A 50-m-thick primary magma intrudes cooler (1000 °C), evolved magma. The results show that the edges of the primary magma would be decreased by 66 °C in 300 days but temperature of the center of primary magma is unaffected.

5.2. Degree and scale of magma undercooling

To quantify the degree and scale of magma undercooling, numerical modeling of 1-D thermal diffusion was carried out using a conductive cooling model and treated as two scenarios, *i.e.*, (1) initial intrusion of parental magma into country rocks, and (2) magma injection into evolved magma. Since we only intend to constrain the thermal histories of magma during the earliest stage of these two scenarios, only the loss of heat through conductive cooling was considered for all modeling; the latent heat of crystallization and convective cooling were ignored. The temperature of parental magma of the Layered Series is set to be 1150 °C (Namur et al., 2010). Given that the Sept Iles intrusion was emplaced into gneisses of the Grenville Province at 1-3 kbar (Higgins, 2005), the temperature of footwall rocks is estimated to be 300 °C assuming the geothermal gradient is 30 °C/km. The Border zone between the footwall rocks and MCU I is at least 20 m thick and composed of fine-grained gabbro, which was thought as a chilled margin (Namur et al., 2010). Thus, the temperature of a border zone is set to be 800 °C. To evaluate the effect of the border zone on thermal evolution at the floor, the thickness of the border zone is set to be 20 and 40 m, respectively.

We evaluate the scenario 1 of hot (1150 °C) parental magma intruding cold (300 °C) footwall rocks with a border zone (800 °C) being 20 m and 40 m in thickness, respectively. For a 20-m-thick border zone, the results reveal that a 2-m-thick magma layer above the border zone would be cooled down by ~40-125 °C in 100 days and a 10-m-thick magma layer would be cooled down by ~25-149 °C in 1000 days (Fig. 6A). The averaged cooling rate is then ~9-54 °C/year at 1000 days, which is much faster than the cooling rate of the lower oceanic crust (0.005 to 0.0001 °C/year, Faak and Gillis, 2016). In 10000 days, a ca. 34-m-thick magma

layer would be cooled down by 25-249 °C (Fig. 6A). For a 40-m-thick border zone, however, the degree of magma undercooling at 10000 days is significantly reduced to a maximum value of ~183 °C (Fig. 6B). However, the thickness of a magma layer that is subjected to minimum degree of undercooling (25 °C; Shea et al., 2019) at 10000 days is 32 m, similar to that for 20-m-thick border zone (Fig. 6A-B). This suggests that high-degree undercooling is very likely to occur in the margin of a magma chamber, facilitating rapid, dendritic growth of olivine in MCU I and that thicker border zone may not significantly reduce the degree of undercooling required for dendritic growth of olivine. The rapidly growing olivine in the margin may be transported by magma convection towards the interior of magma chamber and overgrow with relatively low cooling rate. In addition, the anorthosite in the UBS of the Sept Iles intrusion was considered to have formed by plagioclase flotation during early fractionation of MCU I, and ~13 wt.% plagioclase is missing from the basal troctolite and 16-28 wt.% plagioclase is missing from the Fe-Ti oxide-bearing cumulates of MCU I (Namur et al., 2011). Therefore, we argue that high-degree undercooling in the margin of magma chamber may not only result in rapid growth of olivine but also rapid crystallization of plagioclase, both are crucial to construct the initial crystal framework of MCU I.

In the scenario 2 of primary magma (1150 °C) injecting into evolved magmas above a crystal pile within MCU II, only the maximum temperature difference between them was evaluated here. The temperature of the evolved magma is set to be 1000 °C after the saturation of apatite (Charlier et al., 2011). The modeling results indicate that if a 10-m-thick primary magma layer intrudes the base of evolved magma, the primary magma layer would be cooled down by 23 to 67 °C in 300 days (Fig. 6C), yielding an averaged cooling rate of ~28 °C/year at the center and ~82 °C/year at the edges, respectively. This indicates that injection of small amounts of hot, primary magma into cooler, evolved magma may produce high degrees of undercooling at the edges and low degrees of undercooling at the center of primary magma. In contrast, when a 50-m-thick primary magma layer intrudes the evolved magma, the edges of the layer would be cooled down by 66 °C in 300 days but the temperature of the center would not be changed (Fig. 6D). In this fashion, P-rich dendrites of olivine likely grew along the edges rather than the center of a thick, injecting primary magma layer. However, dynamic mixing and convective cooling in magma chamber can enhance quick and efficient heat loss of mixed magma (Oldenburg et al., 1989). In such a case, undercooling (>25 °C) may be more efficient and extensive in the magma chamber than expected. This may explain the prevalence of dendritic P zoning of olivine in MCU II (Figs. 3–4).

5.3. Cooling rate of the Sept Iles intrusion

Phosphorus zoning of olivine may record the timescale of P diffusion on cooling (Bradshaw et al., 2018; Nelson et al., 2021), and thus can be used to estimate the cooling rate of magma. However, using P zoning of olivine to retrieve the diffusion timescale is still challenging due to uncertainties in the determination of P gradients and diffusivity of P in olivine (Shea et al., 2019; Lynn et al., 2020; Nelson et al., 2020).

We evaluated the sharpness of P gradients of P-rich bands with a wide (>20 μm), high plateau in the olivine grain from MCU II (Fig. 5) via measuring the midpoint slope (S_0) of P gradients following Watson and Cherniak (2015) and Tang et al. (2017). The results show that the outer boundaries of P-rich bands have restricted S_0 of ~25 %/μm, whereas the inner boundaries have S_0 varying from ~10 to 20 %/μm (Fig. 7A-B). The inner boundaries with large variations of S_0 are likely the cutting effect on olivine grains that are randomly orientated in thin sections (Shea et al., 2015), and are thus excluded from diffusion modeling. Here, only the outer boundaries of P-rich bands with wide (>20 μm), high plateau were chosen for diffusion modeling (Fig. 5D-F).

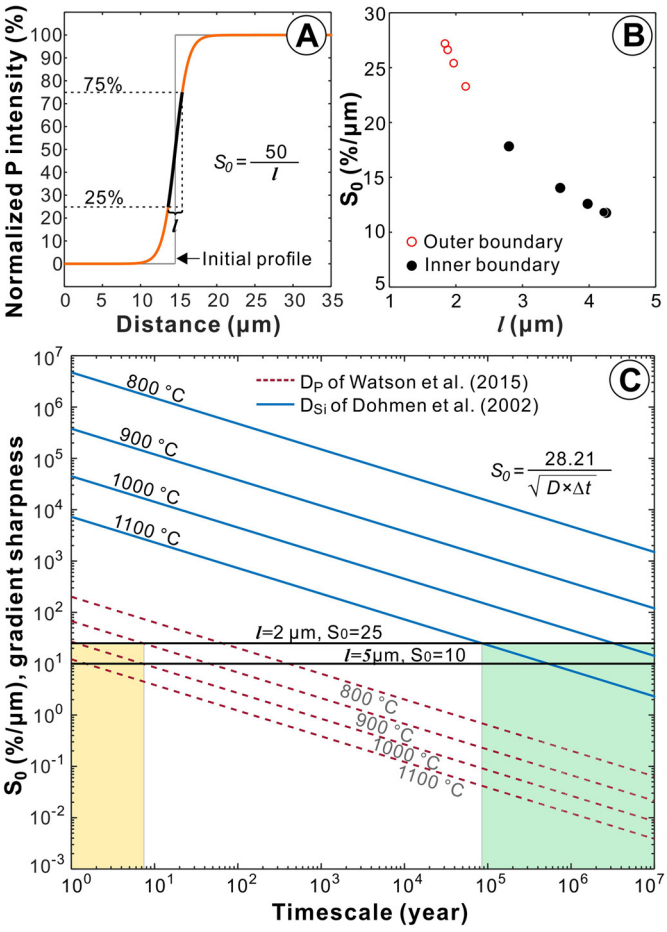

Fig. 7. Midpoint slope (S_0) of P gradients in olivine and the timescale required to preserve the observed P gradients. (**A**) Normalized P intensity profile illustrating the sharpness of P gradient, which can be estimated by measuring S_0 (Watson and Cherniak, 2005). S_0 can be directly determined by measuring the diffusion distance (l) for P intensity variations from 25% to 75% (Tang et al., 2017). (**B**) Results of S_0 for the inner and outer boundaries of P-rich bands in a single olivine in Fig. 5A. The results show that the outer boundaries have a restricted range of S_0 (~25 %/μm), whereas the inner boundaries have a wide range of S_0 (10-20 %/μm). (**C**) The timescale required to preserve the observed P gradients in this study, which was modeled at different temperatures using the diffusivity of Si (Dohmen et al., 2002) and the diffusivity of P (Watson et al., 2015), respectively. The yellow area refers to the timescale required for 25 %/μm S_0 using the diffusivity of P from Watson et al. (2015), which is <8 years at 900 °C. The green area refers to the timescale required for preservation of the same S_0 using the diffusivity of Si from Dohmen et al. (2002), which is >10^6 years at 1000 °C. (For interpretation of the colors in the figure(s), the reader is referred to the web version of this article.)

The timescale of P diffusion in olivine was modeled at constant temperature using the Fick's Second law in one dimension (Crank, 1975), which incorporates two key parameters, *i.e.*, diffusion coefficient of P (D_P) and temperature. So far, the published D_P for olivine was only obtained for Mg-rich San Carlos olivine (Watson et al., 2015), which however was considered to be higher than the actual diffusivity of P in natural olivine (Bradshaw et al., 2018; Nelson et al., 2020, 2021). Using the D_P by Watson et al. (2015), the sharp P gradients in the outer boundaries of P-rich bands observed in this study can be only preserved for <1 year at 1100 °C or <8 years at 900 °C (Fig. 7C). This seems unrealistically too short for the cooling history of the Sept Iles intrusion. Alternatively, we used the diffusion coefficient of Si in olivine to calculate the timescale of P diffusion. As P substitutes Si in the tetrahedral site of olivine (Agrell et al., 1998; Boesenberg and Hewins, 2010), the diffusiv-

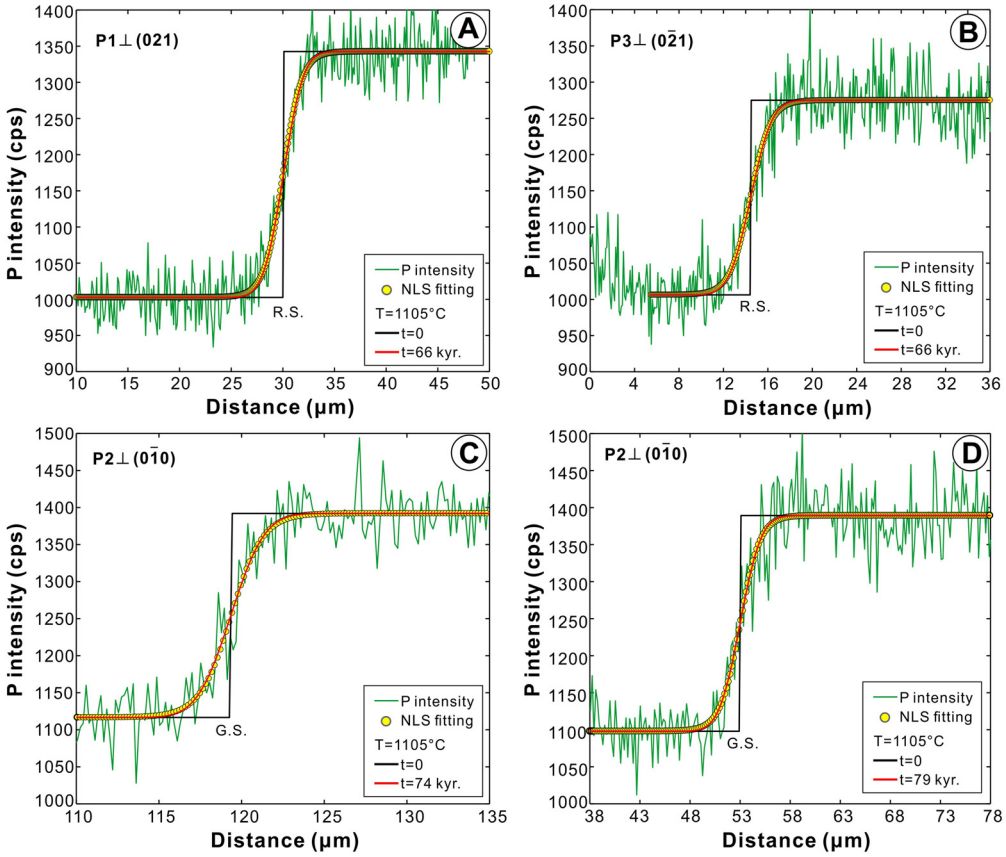

Fig. 8. Timescale obtained by 1D diffusion modeling for the P profiles across different crystal planes of a single olivine grain. The diffusivity of P was adopted using the diffusivity of Si in olivine at 1105 °C (Dohmen et al., 2002). Phosphorus intensity profiles were fitted using nonlinear least squares regression method and then the fitted curves were used for diffusion modeling. The "best fit" was obtained using the minimum root mean squares (rms) method (Girona and Costa, 2013). The results show that the resorption surfaces (R.S.) in plane {0 2 1} and {0$\bar{2}$ 1} are identical to ca. 66 kyr. (A-B), whereas those for growth surfaces (G.S.) in plane {0$\bar{1}$ 0} are longer to ca. 74-79 kyr. (C-D).

ity of P is supposed to be similar to that of Si in olivine (Nelson et al., 2020). The diffusivity of Si is affected by H_2O content of olivine and can be increased by several orders of magnitude in olivine containing tens of ppm H_2O (Supplementary Fig. 7; Costa and Chakraborty, 2008). Here, we tried to measure H_2O content of olivine using a vacuum-type Fourier transform infrared spectrometer (FTIR), the results do not show obvious H_2O peaks in the infrared absorption spectrum (Supplementary Fig. 8), and thus fail to yield precise H_2O content. However, this indicates that the H_2O content of olivine in the Layered Series should be very low. We thus chose the diffusion coefficient of Si in dry olivine (Dohmen et al., 2002) to represent the minimum D_P of olivine, which would result in the maximum value for the diffusion timescale of P in olivine.

Since olivine and plagioclase are liquidus phases in the rocks of the Layered Series, crystallization temperature of olivine was estimated using empirical plagioclase thermometer of Thy et al. (2013). Plagioclase has An content of 56-58 (Supplementary Table 3), the crystallization temperature was then estimated to be ~1105±18 °C (1σ) on average. The closure temperature (T_c) of P in olivine, at which diffusion becomes extremely slow and compositional gradients will be "frozen", can be calculated using the method of Ganguly and Tirone (1999):

$$\frac{E}{RT_c} = \ln\left(-\frac{A'RT_C^2 D_0}{E(dT/dt)_{T_c}a^2}\right) \quad (5)$$

where E and D_0 are the activation energy and pre-exponential factors for the diffusion species, $(dT/dt)_{Tc}$ is the cooling rate at T_c, a is the radius of grain, R is the gas constant. $A' = e^{G+g}$, where e^G is defined as a geometric factor (A), and G = 4.0066 for spheres, 3.29506 for cylinders, and 2.15821 for plane sheets (Dodson, 1973). The term "g" is defined as a "closure function" and is a function of a dimensionless parameter, M, which incorporates cooling rate, grain radius, D (T_0) and E and can be calculated following Ganguly and Tirone (1999):

$$M = \frac{RD(T_0)}{E\eta a^2} \quad (6)$$

where D (T_0) is the diffusion coefficient of species at T_0, η is a cooling time constant with dimension of $K^{-1}t^{-1}$. In this model, cooling is assumed to be asymptotic and given by

$$\frac{1}{T} = \frac{1}{T_0} + \eta t \quad (7)$$

so that $dT/dt = -\eta T^2$. The relationship of g and M is shown in Ganguly and Tirone (1999). For M <10^{-3}, T_c is very close to T_0 (Ganguly and Tirone, 1999). Due to the uncertainty of D_P in olivine, E and D_0 of Si in dry olivine from Dohmen et al. (2002) and those in hydrous olivine from Costa and Chakraborty (2008) were adopted for calculation assuming a sphere geometric factor. The initial temperature (T_0) was set to be 1105 °C. Using the E and D_0 of Si in dry olivine from Dohmen et al. (2002), the calculated M ranges from ~10^{-4} to 10^{-7} for the grains with a radius of 1 mm, so that the T_c is close to the initial temperature. Instead, using E and D_0 of Si in olivine from Costa and Chakraborty (2008), the calculated M is higher than 10^{-3} for the grains with a radius of 1 mm and the

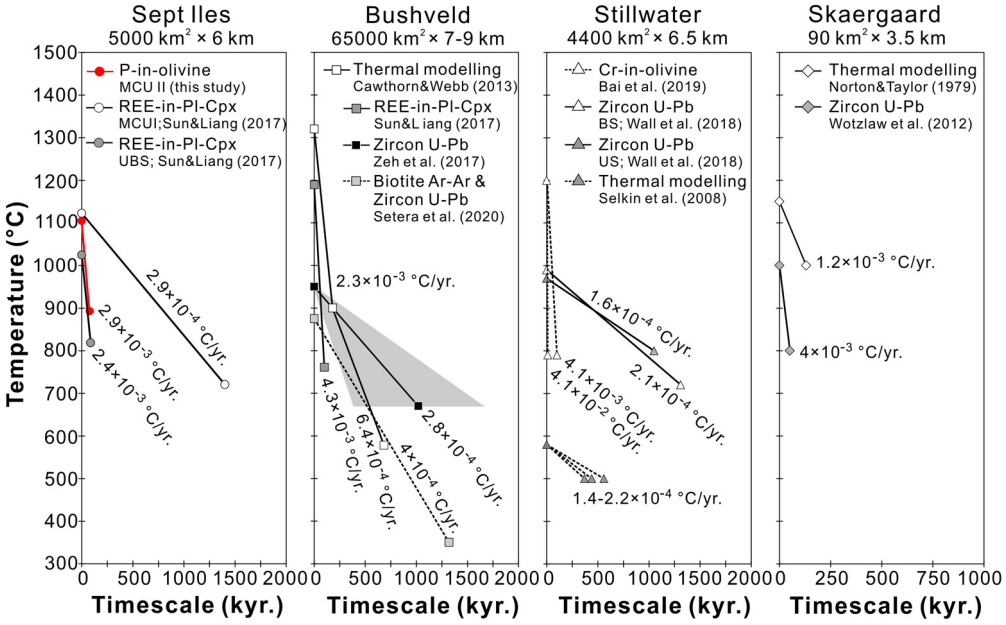

Fig. 9. Comparison of cooling timescale and averaged cooling rate of the Sept Iles, Bushveld, Stillwater and Skaergaard intrusions. The averaged cooling rate for the central part of the Layered Series of the Sept Iles intrusion was estimated to be 2.9×10^{-3} °C/year on average. Note that the diffusivity of Si in dry olivine (Dohmen et al., 2002) was used for that of P, and thus the cooling rate obtained in this study could be a minimum value. The obtained value is comparable with the averaged cooling rate of anorthosite in UBS of the intrusion that was obtained using the REE-in-plagioclase-clinopyroxene thermometer (Sun and Liang, 2017). Combining previously published data of the Bushveld, Stillwater and Skaergaard intrusions, the averaged cooling rate of these intrusions is $\sim10^{-2}$ to 10^{-3} °C/year at temperature of >800 °C. However, the averaged cooling rate decreases by one order of magnitude to $\sim10^{-4}$ °C/year once the temperature decreases below 800 °C. This indicates that rapid cooling of magma could be dominated at high temperature in mafic magma chambers regardless of the scale of magma chambers, and that postcumulus cooling carried on slowly and took much longer time.

resultant T_c is 890 °C at cooling rate of 1 °C/myr. (Supplementary Fig. 9).

The timescale of P diffusion in olivine was then modeled to be in a range of 66 to 79 kyr for the profiles across different crystal planes (Fig. 8). The timescales for the resorption surface (R.S.) in plane {0 2 1} and {$0\overline{2}$ 1} are identical to ca. 66 kyr. (Fig. 8A, B), whereas those for growth surface (G.S.) in plane {$0\overline{1}$ 0} are longer to ca. 74-79 kyr. (Fig. 8C, D). Despite the time differences, our calculation yields an averaged cooling rate of $2.7\text{-}3.3\times10^{-3}$ °C/year (2.9×10^{-3} °C/year on average) in the center of the Layered Series. This value is comparable with the cooling rate of anorthosite in the UBS of the Sept Iles intrusion (Fig. 9), which is based on the REE-in-plagioclase-clinopyroxene thermometer (Sun and Liang et al., 2017). In addition, our result is also similar to the averaged cooling rate of $2.3\text{-}4.3\times10^{-3}$ °C/year for the Bushveld complex (Cawthorn and Webb, 2013; Sun and Liang, 2017), and $1.2\text{-}4\times10^{-3}$ °C/year for the Skaergaard intrusion (Norton and Taylor, 1979; Wotzlaw et al., 2012) (Fig. 9). However, it is slightly slower than the cooling rate of 4.1×10^{-2} - 10^{-3} °C/year for the Stillwater complex in USA (Bai et al., 2019) (Fig. 9). Overall, the similarity in the averaged cooling rates of these different-scale layered intrusions indicates that rapid cooling (ca. 10^{-2} to 10^{-3} °C/year) at high temperature (>800 °C) may be predominant regardless of the size of magma chamber. In addition, previous studies show that the cooling rates of the Sept Iles, Bushveld and Stillwater intrusions decrease by one order of magnitude to $\sim10^{-4}$ °C/year when temperature drops below 800 °C (Fig. 9), indicating that the postcumulus cooling may take much longer time.

5.4. Implications for crystallization and cooling histories of crustal magma chambers

Our study provides direct evidence for dendritic growth of olivine throughout the Layered Series of the Sept Iles intrusion, indicating that dendritic growth of olivine may be ubiquitous in mafic magma chambers, challenging the conventional "tree-ring" growth model of olivine under near-equilibrium conditions. The widespread P-rich dendrites and skeletons of olivine and particularly those in the interior of the Layered Series also argue that large mafic magma chambers may have experienced fast cooling in the initial stage.

Experimental results reveal that the growth rate of olivine is $\sim10^{-7}$ to 10^{-8} m/s at moderate undercooling (40-60 °C) and phenocryst-size olivine frameworks can be formed in 1 to 2 hours (Mourey and Shea, 2019), much faster than that of olivine in near-equilibrium growth (10^{-10} m/s) under low degree of undercooling (10-15 °C, Jambon et al., 1992). Under moderate undercooling, a 2-mm-sized olivine as observed in the Sept Iles intrusion may grow up in ca. 3-30 hours, whereas an olivine grain of the same size may take ca. 116 days to grow up under near-equilibrium condition. This indicates that growth of olivine could be instantaneous in the parts of magma chamber with similar undercooling regime. In the Sept Iles intrusion, magma undercooling at the boundary layer of magma with high thermal contrast may have induced rapid growth of both olivine and plagioclase. Plagioclase laths that grew fast at the base of magma chamber may float up towards the top of magma chamber, forming anorthosite of the UBS (Namur et al., 2011). Therefore, it is very likely that the dendritic olivine and plagioclase that formed by rapid growth may construct the initial mushy state of the magma chamber.

An unexpected feature in all olivine grains examined in this study is that the P-rich zones of olivine experienced variable degrees of dissolution (Figs. 2–5 and Supplementary Figs. 2-4). These complex P zoning patterns actually record a two-stage growth process of olivine, *i.e.*, initially dendritic/skeletal growth and ripening, followed by late-stage dissolution and reprecipitation. Similar textures were also documented for the olivine in the Baima layered intrusion that hosts economic Fe-Ti oxide deposit in SW China (Xing et al., 2017). It is also noted that the magnetite and sulfides are all enclosed within P-poor olivine domains (Figs. 2G and

4F), indicating that late-stage dissolution should occur before crystallization of magnetite and saturation of sulfides. The dissolution process was likely triggered by the evolved interstitial melt that may have become Fe-rich and in chemical disequilibrium with early crystallized olivine. The chemical disequilibrium between the interstitial melt and primocrysts in mush has been recognized in the Sept Iles intrusion, shown by distinct replacive symplectites on plagioclase primocrysts due to silicate liquid immiscibility (Namur et al., 2012; Keevil et al., 2020). In addition, olivine grains in the apatite olivine gabbro at the top of MCU I and the apatite troctolite and olivine nelsonite at the top of MCU II have low Fo contents of ~49 to 54, but they also show intense dissolution of P-rich zones. Relatively large apatite grains are partially enclosed within P-poor rims of the grains (Figs. 2I, 3F-G and Supplementary Fig. 3), indicating that P-rich, dendritic/skeletal olivine crystallized earlier than apatite saturation of magma. During solidification of crystal frameworks, enhanced release of latent heat of crystallization may significantly buffer the decrease of liquidus temperature of the interstitial melt (Namur et al., 2014), and even lead to recalescence or spontaneous reheating of cooling materials at extremely fast cooling conditions (Whittington and Sehlke, 2021). This may slow down postcumulus cooling, consequently, overgrowth of P-poor olivine domains may take place slowly due to significantly reducing undercooling and thus decreasing growth rate of olivine. This also explains the absence of P zoning in the olivine from anorthosite of MCU I (Supplementary Fig. 5) because the olivine crystallized from evolved interstitial liquid. Our study reveals that P zoning of olivine can be powerful tools to decode the high-temperature crystallization and cooling histories of mafic-ultramafic intrusions elsewhere.

6. Conclusions

High resolution elemental mapping of olivine from the Sept Iles layered intrusion shows complex P zoning of olivine throughout the ~4.7-km Layered Series. The P-rich zones within a single olivine grain occur as dendritic, hopper and sector patterns, which are commonly corroded by P-poor olivine domains. The P zoning of olivine reveals ubiquitous dendritic growth of olivine in a large mafic magma chamber, followed by dissolution and reprecipitation processes. Initial intrusion of hot parental magma into cold country rocks could result in high degrees of undercooling in the margin of magma chambers, facilitating rapid growth of olivine, which is crucial to construct the initial crystal framework of MCU I. Replenishment of primary magma into evolved residual magma and magma mixing may play a significant role in inducing widespread dendritic growth of olivine in MCU II. The minimum cooling rate is 2.7 to 3.3×10^{-3} °C/year in the center of the Layered Series of the Sept Iles intrusion, indicating rapid cooling of magma at high temperature in this large mafic magma chamber.

CRediT authorship contribution statement

C.-M. Xing: Conceptualization, Data curation, Investigation, Methodology, Writing - original draft, Writing - review & editing. **C.Y. Wang:** Conceptualization, Funding acquisition, Writing - review & editing. **B. Charlier:** Conceptualization, Sample collection, Writing - review & editing. **O. Namur:** Sample collection, Writing - review & editing.

Declaration of competing interest

The authors declare that they have no known competing financial interests or personal relationships that could have appeared to influence the work reported in this paper.

Acknowledgements

This study was financially supported by the National Key R&D Program of China (2018YFA0702600), NSFC grants (42072068, 41921003 and 41325006), the Youth Innovation Promotion Association CAS (2018388), and Science and Technology Planning of Guangdong Province, China (2020B1212060055). BC is a Research Associate of the Belgian Fund for Scientific Research-FNRS. Many thanks to Jibamitra Ganguly, who kindly guided the calculation of closure temperature. William Nelson was thanked for his suggestion for the diffusivity of P in olivine. Valentina Batanova kindly shared the MongOL Sh11-2 olivine standard. Wei Tan and Jiang-Ze Wang were thanked for providing assistance during EBSD analysis and measurement of modal proportion of minerals. Eiichi Takahashi was thanked for helping FTIR analysis. We are grateful to Christian Tegner and one anonymous reviewer, and editor, Chiara Maria Petrone, who kindly provided constructive comments that were helpful to improve the manuscript.

Appendix A. Supplementary material

Supplementary material related to this article can be found online at https://doi.org/10.1016/j.epsl.2022.117710.

References

Agrell, S.O., Charnley, N.R., Chinner, G.A., 1998. Phosphoran olivine from Pine Canyon, Piute Co., Utah. Mineral. Mag. 62.
Bachmann, F., Hielscher, R., Schaeben, H., 2010. Texture analysis with MTEX – free and open source software toolbox. Solid State Phenom. 160, 63–68.
Bai, Y., Su, B.-X., Xiao, Y., Chen, C., Cui, M.-M., He, X.-Q., Qin, L.-P., Charlier, B., 2019. Diffusion-driven chromium isotope fractionation in ultramafic cumulate minerals: elemental and isotopic evidence from the Stillwater Complex. Geochim. Cosmochim. Acta 263, 167–181.
Batanova, V.G., Thompson, J.M., Danyushevsky, L.V., Portnyagin, M.V., Garbe-Schönberg, D., Hauri, E., Kimura, J.-I., Chang, Q., Senda, R., Goemann, K., Chauvel, C., Campillo, S., Ionov, D.A., Sobolev, A.V., 2019. New olivine reference material for in situ microanalysis. Geostand. Geoanal. Res. 43, 453–473.
Boesenberg, J.S., Hewins, R.H., 2010. An experimental investigation into the metastable formation of phosphoran olivine and pyroxene. Geochim. Cosmochim. Acta 74, 1923–1941.
Bradshaw, R.W., Kent, A.J.R., Tepley III, F.J., 2018. Chemical fingerprints and residence times of olivine in the 1959 Kilauea Iki eruption, Hawaii: insights into picrite formation. Am. Mineral. 103, 1812–1826.
Brandeis, G., Jaupart, C., 1986. On the interaction between convection and crystallization in cooling magma chambers. Earth Planet. Sci. Lett. 77, 345–361.
Cashman, K.V., Sparks, R.S.J., Blundy, J.D., 2017. Vertically extensive and unstable magmatic systems: a unified view of igneous processes. Science 355, eaag3055.
Cawthorn, R.G., Webb, S.J., 2013. Cooling of the Bushveld Complex, South Africa: implications for paleomagnetic reversals. Geology 41, 687–690.
Charlier, B., Namur, O., Toplis, M.J., Schiano, P., Cluzel, N., Higgins, M.D., Auwera, J.V., 2011. Large-scale silicate liquid immiscibility during differentiation of tholeiitic basalt to granite and the origin of the Daly gap. Geology 39, 907–910.
Costa, F., Chakraborty, S., 2008. The effect of water on Si and O diffusion rates in olivine and implications for transport properties and processes in the upper mantle. Phys. Earth Planet. Inter. 166, 11–29.
Crank, J., 1975. The Mathematics of Diffusion, 2ed ed. Oxford Science Publications, Oxford.
de Maisonneuve, C.B., Costa, F., Huber, C., Vonlanthen, P., Bachmann, O., Dungan, M.A., 2016. How do olivines record magmatic events? Insights from major and trace element zoning. Contrib. Mineral. Petrol. 171, 56.
Di Maio, R., Piegari, E., Mancini, C., Scandone, R., 2015. Numerical study of conductive heat losses from a magmatic source at Phlegraean Fields. J. Volcanol. Geotherm. Res. 290, 75–81.
Dohmen, R., Chakraborty, S., Becker, H.-W., 2002. Si and O diffusion in olivine and implications for characterizing plastic flow in the mantle. Geophys. Res. Lett. 29, 26–21–26-24.
Donaldson, C.H., 1976. An experimental investigation of olivine morphology. Contrib. Mineral. Petrol. 57, 187–213.
Faak, K., Gillis, K.M., 2016. Slow cooling of the lowermost oceanic crust at the fast-spreading East Pacific Rise. Geology 44, 115–118.
Faure, F., Schiano, P., 2005. Experimental investigation of equilibration conditions during forsterite growth and melt inclusion formation. Earth Planet. Sci. Lett. 236, 882–898.

Faure, F., Schiano, P., Trolliard, G., Nicollet, C., Soulestin, B., 2007. Textural evolution of polyhedral olivine experiencing rapid cooling rates. Contrib. Mineral. Petrol. 153, 405–416.
Faure, F., Trolliard, G., Nicollet, C., Montel, J.-M., 2003. A developmental model of olivine morphology as a function of the cooling rate and the degree of undercooling. Contrib. Mineral. Petrol. 145, 251–263.
Ganguly, J., Tirone, M., 1999. Diffusion closure temperature and age of a mineral with arbitrary extent of diffusion: theoretical formulation and applications. Earth Planet. Sci. Lett. 170, 131–140.
Girona, T., Costa, F., 2013. DIPRA: a user-friendly program to model multi-element diffusion in olivine with applications to timescales of magmatic processes. Geochem. Geophys. Geosyst. 14, 422–431.
Higgins, M.D., 2005. A new interpretation of the structure of the Sept Iles Intrusive suite, Canada. Lithos 83, 199–213.
Higgins, M.D., van Breemen, O., 1998. The age of the Sept Iles layered mafic intrusion, Canada: implications for the late Neoproterozoic/Cambrian history of Southeastern Canada. J. Geol. 106, 421–432.
Holness, M.B., Tegner, C., Nielsen, T.F., Stripp, G., Morse, S.A., 2007. A textural record of solidification and cooling in the Skaergaard intrusion, East Greenland. J. Petrol. 48, 2359–2377.
Irvine, T.N., Andersen, J.C.Ø., Brooks, C.K., 1998. Included blocks (and blocks within blocks) in the Skaergaard intrusion: geologic relations and the origins of rhythmic modally graded layers. GSA Bull. 110, 1398–1447.
Jambon, A., Lussiez, P., Clocchiatti, R., Weisz, J., Hernandez, J., 1992. Olivine growth rates in a tholeiitic basalt: an experimental study of melt inclusions in plagioclase. Chem. Geol. 96, 277–287.
Keevil, H.A., Namur, O., Holness, M.B., 2020. Microstructures and late-stage magmatic processes in layered mafic intrusions: symplectites from the Sept Iles intrusion, Quebec, Canada. J. Petrol. 61, egaa071.
Latypov, R., Chistyakova, S., Barnes, S.J., Godel, B., Delaney, G.W., Cleary, P.W., Radermacher, V.J., Campbell, I., Jakata, K., 2022. Chromitite layers indicate the existence of large, long-lived, and entirely molten magma chambers. Sci. Rep. 12, 4092.
Latypov, R.M., Chistyakova, S.Y., Namur, O., Barnes, S., 2020. Dynamics of evolving magma chambers: textural and chemical evolution of cumulates at the arrival of new liquidus phases. Earth-Sci. Rev. 210, 103388.
Loncarevic, B.D., Feininger, T., Lefebvre, D., 1990. The Sept-îles layered mafic intrusion: geophysical expression. Can. J. Earth Sci. 27, 501–512.
Lynn, K.J., Garcia, M.O., Shea, T., 2020. Phosphorus coupling obfuscates lithium geospeedometry in Olivine. Front. Earth Sci. 8.
Mao, Y.-J., Schoneveld, L., Barnes, S.J., Williams, M.J., Su, B.-X., Ruprecht, P., Evans, N.J., Qin, K.-Z., 2022. Coupled Li-P zoning and trace elements of olivine from magmatic Ni-Cu deposits: implications for postcumulus re-equilibration in olivine. J. Petrol. 63, egac018.
McBirney, A.R., 1996. The Skaergaard intrusion. In: Cawthorn, R.G. (Ed.), Developments in Petrology. Elsevier, pp. 147–180.
Milman-Barris, M.S., Beckett, J.R., Baker, M.B., Hofmann, A.E., Morgan, Z., Crowley, M.R., Vielzeuf, D., Stolper, E., 2008. Zoning of phosphorus in igneous olivine. Contrib. Mineral. Petrol. 155, 739–765.
Morse, S.A., 1986. Thermal structure of crystallizing magma with two-phase convection. Geol. Mag. 123, 205–214.
Mourey, A.J., Shea, T., 2019. Forming olivine phenocrysts in basalt: a 3D characterization of growth rates in laboratory experiments. Front. Earth Sci. 7.
Namur, O., Charlier, B., Holness, M.B., 2012. Dual origin of Fe-Ti-P gabbros by immiscibility and fractional crystallization of evolved tholeiitic basalts in the Sept Iles layered intrusion. Lithos 154, 100–114.
Namur, O., Charlier, B., Pirard, C., Hermann, J., Liégeois, J.-P., Auwera, J.V., 2011. Anorthosite formation by plagioclase flotation in ferrobasalt and implications for the lunar crust. Geochim. Cosmochim. Acta 75, 4998–5018.
Namur, O., Charlier, B., Toplis, M.J., Higgins, M.D., Liégeois, J.-P., Vander Auwera, J., 2010. Crystallization sequence and magma chamber processes in the ferrobasaltic Sept Iles layered intrusion, Canada. J. Petrol. 51, 1203–1236.
Namur, O., Humphreys, M.C.S., Holness, M.B., 2014. Crystallization of interstitial liquid and latent heat buffering in solidifying gabbros: Skaergaard intrusion, Greenland. J. Petrol. 55, 1389–1427.
Nelson, W.S., Hammer, J.E., Shea, T., Hellebrand, E., Jeffrey Taylor, G., 2021. Chemical heterogeneities reveal early rapid cooling of Apollo Troctolite 76535. Nat. Commun. 12, 7054.
Nelson, W., Hammer, J., Shea, T., Chakraborty, S., 2020. Diffusivity of phosphorous in olivine revisited: a joint experimental and modeling approach. In: Goldschmidt Conference Abstracts.
Norton, D., Taylor Jr., H.P., 1979. Quantitative simulation of the hydrothermal systems of crystallizing magmas on the basis of transport theory and oxygen isotope data: an analysis of the Skaergaard intrusion. J. Petrol. 20, 421–486.
Oldenburg, C.M., Spera, F.J., Yuen, D.A., Sewell, G., 1989. Dynamic mixing in magma bodies: theory, simulations, and implications. J. Geophys. Res., Solid Earth 94, 9215–9236.
Shea, T., Costa, F., Krimer, D., Hammer, J.E., 2015. Accuracy of timescales retrieved from diffusion modeling in olivine: a 3D perspective. Am. Mineral. 100, 2026–2042.
Shea, T., Hammer, J.E., 2013. Kinetics of cooling- and decompression-induced crystallization in hydrous mafic-intermediate magmas. J. Volcanol. Geotherm. Res. 260, 127–145.
Shea, T., Hammer, J.E., Hellebrand, E., Mourey, A.J., Costa, F., First, E.C., Lynn, K.J., Melnik, O., 2019. Phosphorus and aluminum zoning in olivine: contrasting behavior of two nominally incompatible trace elements. Contrib. Mineral. Petrol. 174, 85.
Sparks, R.S.J., Cashman, K.V., 2017. Dynamic magma systems: implications for forecasting volcanic activity. Elements 13, 35–40.
Streck, M.J., 2008. Mineral textures and zoning as evidence for open system processes. Rev. Mineral. Geochem. 69, 595–622.
Sun, C., Liang, Y., 2017. A REE-in-plagioclase–clinopyroxene thermometer for crustal rocks. Contrib. Mineral. Petrol. 172, 24.
Tang, M., Rudnick, R.L., McDonough, W.F., Bose, M., Goreva, Y., 2017. Multi-mode Li diffusion in natural zircons: evidence for diffusion in the presence of step-function concentration boundaries. Earth Planet. Sci. Lett. 474, 110–119.
Tegner, C., Wilson, J.R., 1995. Textures in a poikilitic olivine gabbro cumulate: evidence for supercooling. Mineral. Petrol. 54, 161–173.
Tegner, C., Wilson, J.R., Brooks, C.K., 1993. Intraplutonic quench zones in the Kap Edvard Holm layered gabbro complex, East Greenland. J. Petrol. 34, 681–710.
Thy, P., Lesher, C.E., Tegner, C., 2009. The Skaergaard liquid line of descent revisited. Contrib. Mineral. Petrol. 157, 735–747.
Thy, P., Lesher, C.E., Tegner, C., 2013. Further work on experimental plagioclase equilibria and the Skaergaard liquidus temperature. Am. Mineral. 98, 1360–1367.
Wager, L., Brown, G., 1968. Layered Igneous Rocks. Oliver and Boyd, Edinburgh.
Watson, E.B., Cherniak, D., Holycross, M., 2015. Diffusion of phosphorus in olivine and molten basalt. Am. Mineral. 100, 2053–2065.
Watson, E.B., Cherniak, D.J., 2015. Quantitative cooling histories from stranded diffusion profiles. Contrib. Mineral. Petrol. 169, 57.
Welsch, B., Faure, F., Famin, V., Baronnet, A., Bachèlery, P., 2013. Dendritic crystallization: a single process for all the textures of olivine in basalts? J. Petrol. 54, 539–574.
Welsch, B., Hammer, J., Hellebrand, E., 2014. Phosphorus zoning reveals dendritic architecture of olivine. Geology 42, 867–870.
Whittington, A.G., Sehlke, A., 2021. Spontaneous reheating of crystallizing lava. Geology 49, 1457–1461.
Wotzlaw, J.-F., Bindeman, I.N., Schaltegger, U., Brooks, C.K., Naslund, H.R., 2012. High-resolution insights into episodes of crystallization, hydrothermal alteration and remelting in the Skaergaard intrusive complex. Earth Planet. Sci. Lett. 355–356, 199–212.
Xing, C.-M., Wang, C.Y., Tan, W., 2017. Disequilibrium growth of olivine in mafic magmas revealed by phosphorus zoning patterns of olivine from mafic–ultramafic intrusions. Earth Planet. Sci. Lett. 479, 108–119.
Yao, Z., Mungall, J.E., Jenkins, M.C., 2021. The Rustenburg Layered Suite formed as a stack of mush with transient magma chambers. Nat. Commun. 12, 505.

Further reading

Selkin, P.A., Gee, J.S., Meurer, W.P., Hemming, S.R., 2008. Paleointensity record from the 2.7 Ga Stillwater Complex, Montana. Geochem. Geophys. Geosyst. 9, Q12023.
Setera, J.B., VanTongeren, J.A., Turrin, B.D., Swisher III, C.C., 2020. Rapid cooling of the Rustenburg Layered Suite of the Bushveld Complex (South Africa): insights from biotite $^{40}Ar/^{39}Ar$ geochronology. Geology 48, 834–838.
Wall, C.J., Scoates, J.S., Weis, D., Friedman, R.M., Amini, M., Meurer, W.P., 2018. The Stillwater Complex: integrating zircon geochronological and geochemical constraints on the age, emplacement history and crystallization of a large, open-system layered intrusion. J. Petrol. 59, 153–190.
Zeh, A., Ovtcharova, M., Wilson, A.H., Schaltegger, U., 2015. The Bushveld Complex was emplaced and cooled in less than one million years – results of zirconology, and geotectonic implications. Earth Planet. Sci. Lett. 418, 103–114.